Research article

Debabrata Sikdar* and Alexei A. Kornyshev

An electro-tunable Fabry–Perot interferometer based on dual mirror-on-mirror nanoplasmonic metamaterials

https://doi.org/10.1515/nanoph-2019-0317
Received August 16, 2019; revised September 10, 2019; accepted October 1, 2019

Abstract: Mirror-on-mirror nanoplasmonic metamaterials, formed on the basis of voltage-controlled reversible self-assembly of sub-wavelength-sized metallic nanoparticles (NPs) on thin metallic film electrodes, are promising candidates for novel electro-tunable optical devices. Here, we present a new design of electro-tunable Fabry–Perot interferometers (FPIs) in which two parallel mirrors – each composed of a monolayer of NPs self-assembled on a thin metallic electrode – form an optical cavity, which is filled with an aqueous solution. The reflectivity of the cavity mirrors can be electrically adjusted, simultaneously or separately, via a small variation of the electrode potentials, which would alter the inter-NP separation in the monolayers. To investigate optical transmittance from the proposed FPI device, we develop a nine-layer-stack theoretical model, based on our effective medium theory and multi-layer Fresnel reflection scheme, which produces excellent match when verified against full-wave simulations. We show that strong plasmonic coupling among silver NPs forming a monolayer on a thin silver-film substrate makes reflectivity of each cavity mirror highly sensitive to the inter-NP separation. Such a design allows the continuous tuning of the multiple narrow and intense transmission peaks emerging from an FPI cavity via electro-tuning the inter-NP separation in situ – reaping the benefits from both inexpensive bottom-up fabrication and energy-efficient tuning.

Keywords: Fabry–Perot interferometers; electro-tunable optical devices; self-assembled plasmonic nanoparticles; voltage-controlled reversible self-assembly.

1 Introduction

A Fabry–Perot interferometer (FPI) is an optical cavity comprising two parallel reflective surfaces, which allows only specific wavelengths of incident light to be transmitted – those satisfying the constructive interference condition within the cavity [1, 2]. The resulting sharp transmission peaks, arising from multiple beam interference within the cavity, are strongly dependent on the construction of the cavity: length, filling material, and reflectivity, of each cavity mirror [1–4]. Tuning of the transmission peaks of FPIs is particularly interesting for applications in spectrometry, wavelength-selective filters, fibre-optic sensors, angle metrology, spectroscopic systems for gas analysis, and biological, chemical, and vibration sensing, just to name a few [5–17].

Most of the works reported in the literature for achieving a tunable FPI involve either alteration of the length of the resonator cavity via a moveable mirror or by inducing change in the refractive index of the material inside the cavity via thermal, electrical, piezoelectric, or other means [12, 17–19]. In several previous works, electrical tuning of the transmittance spectrum of FPIs is achieved by the virtue of the electro-optic and/or piezoelectric effects – through the use of liquid crystals, silicon-based on-chip design, hybrid sol-gel methods, etc. [20–25]. Besides, there have been a few reports on micro-machined MEMS (micro-electromechanical system)-based FPIs, but those structures require expensive and complicated top-down fabrication procedures; moreover, some of them involve relatively large potentials (up to several tens of volts) for tuning the transmitted light wavelength [26–30].

***Corresponding author: Debabrata Sikdar,** Department of Chemistry, Imperial College London, Molecular Sciences Research Hub, White City, W12 0BZ London, UK; and Department of Electronics and Electrical Engineering, Indian Institute of Technology Guwahati, Guwahati 781039, India, e-mail: deb.sikdar@iitg.ac.in. https://orcid.org/0000-0003-3399-9407
Alexei A. Kornyshev: Department of Chemistry, Imperial College London, Molecular Sciences Research Hub, White City, W12 0BZ London, UK; and Thomas Young Centre for Theory and Simulation of Materials, Imperial College London, SW7 2AZ London, UK

Open Access. © 2019 Debabrata Sikdar et al., published by De Gruyter. This work is licensed under the Creative Commons Attribution 4.0 Public License.

FPIs with a large operating voltage can increase the risk of degradation of the device and restrict its usage in many energy-efficient and miniaturized applications. Therefore, it would be interesting to explore an alternative approach that brings together the benefits of inexpensive bottom-up design along with energy efficiency by enabling tuning of the transmission wavelength of an FPI with ultra-low voltage variation.

In this article, we propose a structure and discuss methods for developing tunable FPIs with a simple design, based on voltage-guided self-assembly/disassembly of Ag nanoparticles (NPs) at thin silver film electrodes. The system will allow electrical tuning of the reflectivity of the cavity mirrors, with small (sub-volt) variation of electrode potentials. This work presents an electro-tunable FPI cavity formed between dual mirror-on-mirror nanoplasmonic metamaterials. The proposed design ensures superior transmittance characteristics of an FPI (with narrow, intense, and widely tunable transmission peaks), not achieved in our previous work [31] – involving voltage-controlled self-assembly of gold NPs on transparent electrodes. Those transparent electrodes played no significant role in the cavity's optical properties. The cavity mirrors were realized solely by monolayers of gold NPs. Though electro-tunability could be achieved, weak reflectivity of those cavity mirrors did not allow the formation of a strong optical resonator between them. The transmission peaks obtained there were found to be very broad, spectrally overlapping, and reduced in intensity (due to high loss in gold). These drawbacks of the previous design would limit major applications of an FPI.

Here, we consider mirror-on-mirror nanoplasmonic metamaterials as tunable cavity mirrors for FPIs. Generally, such materials, formed by voltage-controlled assembly/disassembly of metallic NPs on metallic substrates, enable switching between "mirror" and "absorber" states of the metallic substrate [32–35]. A positively polarized metallic substrate, acting as an electrode, can attract negatively charged NPs (charge comes from the attached ligands [36]) from the electrolytic solution, leading to the formation of an adsorbed two-dimensional (2D) array (a "sub-monolayer or dense monolayer") of NPs. Under appropriate positive polarization, the NPs electrosorb strongly on the electrode and get closer to each other, forming a dense monolayer; on a thick metallic substrate, this will result in an "absorber" state with minimum reflectance at certain wavelengths. The wavelength of the absorption peak can be tuned by altering the inter-NP separation via changing the electrode potential. On the other hand, with negative electrode potential, the NPs can be repelled from the electrodes to disassemble into the solution, which unveils the "mirror" or reflective state of the metallic substrate. Here we propose to carefully exploit the state of positively polarized metallic electrodes in order to control the NP density (or the inter-NP separation) in the monolayers to be able to change the reflectivity of the cavity mirrors at different levels of positive potentials.

In the subsequent sections, we present a theory of the optical response of the proposed system and discuss the obtained results, which are then verified against full-wave simulations. Our theoretical findings demonstrate that mirror-on-mirror nanoplasmonic metamaterials can efficiently function as tunable reflective surfaces for realizing electro-tunable FPIs and could be promising in numerous applications.

2 Proposed scheme

We consider two ultra-thin, homogeneous metallic films of thickness around a few tens of nanometres as basic components of the cavity mirrors. The film thickness is chosen such that there is strong reflection from each mirror but they still allow enough transparency to the incoming light for entering and then exiting the cavity. The cavity formed between two such films contains an aqueous electrolyte solution with metallic NPs. The NPs are capped with appropriate ligands whose free ends tend to dissociate in the solution, acquiring negative changes to the ends of those ligands (the degree of ionization can be controlled by the pH) [36–39]. The primary purpose of functionalization of NPs with charged ligands is to overpower their Van der Waals attraction and to avoid agglomeration of NPs in the bulk and also when they are adsorbed at the interface [40]. Most importantly, charging the NPs gives a unique opportunity for a controlled electrosorption/electro-desorption of NPs to/from the electrodes: negatively charged NPs can then be attracted to assemble into a 2D monolayer on a positively polarized metallic film, thus forming a mirror-on-mirror metamaterial at each end of the cavity [33, 34].

These mirror-on-mirror nanoplasmonic metamaterials can act as tunable cavity mirrors. By minute alteration of the positive polarization applied to the thin film electrodes, the inter-NP separation ("gap") within the assembly of NPs on top of the metallic films can be changed *at will*. This change in the density of the NP monolayer coupled to a metallic film, in turn, affects the overall reflectivity of the cavity mirrors and thus allows the transmittance peaks of the cavity to be continuously tuned.

Figure 1 shows different structures for realizing our proposed FPIs with dual mirror-on-mirror plasmonic metamaterials as cavity mirrors, where these mirrors, based on metallic thin-film electrodes can be of any geometric shape, e.g. rectangle, square, polygon, or circle (ellipsoid). The lateral dimensions of the cavity mirrors should be larger than the width of the incoming beam. So, those dimensions can be made very small depending on how small the beam width of the incoming light is. Depending on a specific application's requirement, one can choose the lateral dimensions of those cavity mirrors to be as small as a few micrometres or as large as centimetres and even beyond.

In this work, the two thin-film electrodes are connected to work as a single positive electrode. However, each of those electrodes may also be individually polarized, allowing the cavity configuration [1] to be "under-coupled" or "over-coupled" in contrast to being "critically coupled" where the two electrodes are electrically connected, as shown in Figure 1. The remaining walls of the cavity are insulating materials, containing an embedded frame acting as the counter-electrode.

Note that, if we want such system to operate at low voltages, we need to concentrate the potential drops near electrodes in electrical double layers. That means using electrolytic solutions as media in which the NPs are initially dissolved and from which they adsorb onto the electrode for the corresponding electrode potentials (for negatively charged NPs, these should be positively charged electrodes); this phenomenon is called *electrosorption*. Thus, for just below 1 V electrode potential with respect to its potential of zero charge, the electric field confined within the electrical double layer will be substantial to electrosorb NPs [40].

The thickness of the double layer depends on the electrolyte concentration, which is roughly inversely proportional to the square root of concentration [40]. We cannot make the latter too high because the double layer will be too thin and the electric field will interact only with a small number of charged ligands facing the electrode. But more importantly, we cannot deal with too concentrated solutions for another reason. The Debye screening of Coulomb repulsion between the likely charged NPs in the bulk will be too strong and will not be able to prevent aggregation of NPs driven by Van der Waals forces. Theoretical estimates [40] and experiments [33, 37, 38] suggest that in aqueous solutions it is better not to go beyond 10 mM electrolyte concentrations.

The "price" for concentrating the voltage drops at electrodes, resulting in large electric fields acting on NPs, is that in such configurations there is no electric field in the bulk and the NPs will not migrate but need to reach their potential wells at the electrodes by random diffusion. In macro-sized electrochemical cells, this may take a long time, and, as was shown in Ref. [37], that time is inversely proportional to the square of the cell length. But in the device that we consider here, the cavity length will be of micrometre size, and thus the switching time of the device will be of the order of milliseconds. The theory we present in this article does not address any kinetic aspects of the functioning of this device; however, in similar systems, those have been studied extensively in the previous works of our group [33, 34, 37].

3 Theoretical framework

To describe the optical response of our proposed system, we developed a theoretical framework based on a nine-layer-stack model (Figure 2), which combines our effective medium theory with multi-layer Fresnel

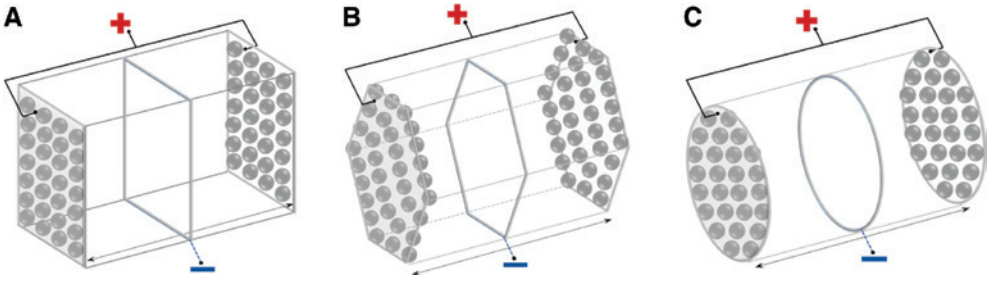

Figure 1: Schematics of the proposed electro-tunable Fabry–Perot interferometers comprising dual mirror-on-mirror nanoplasmonic metamaterials as the cavity mirrors, where the cavity is filled with an aqueous solution of nanoparticles.
Nanoparticles capped with negatively charged ligands assemble on positively polarized thin metallic film electrodes of (A) rectangular/square, (B) polygon, or (C) circular shape, forming electrically tunable mirror-on-mirror metamaterials. The frames shown in the middle of the insulating cavity side walls act as the negatively polarized electrodes.

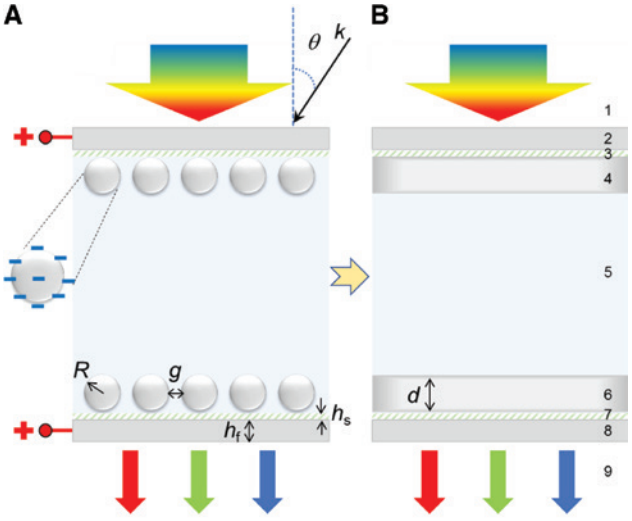

Figure 2: (A) Schematic of the proposed Fabry–Perot interferometer cavity and (B) its equivalent theoretical nine-layer-stack model. Parameters: R, radius of the NPs; g, inter-NP separation; h_s, thickness of the spacer layer; h_f, thickness of the metallic film electrodes; L, cavity length; d, thickness of the effective film emulating an NP monolayer; and k, the wave vector of light incident at angle θ.

reflection scheme [32, 41]. The relative permittivities of layers 1 and 9, representing the media through which light enters and exits the FPI device, are denoted by ε_1 and ε_9, respectively. These two layers may be identical or different, depending on the application. Layers 2 and 8 represent the thin metallic film electrodes of thickness h_f, which are denoted by frequency-dependent permittivities $\varepsilon_2(\omega)$ and $\varepsilon_8(\omega)$, respectively. Layers 3 and 7, representing the spacer layers of thickness h_s between the NPs and their substrates (thin metallic films), are assigned permittivities ε_3 and ε_7, respectively. Layers 4 and 6 emulate the monolayer of NPs, which are modeled as effective films, each of thickness d, with frequency-dependent permittivities $\varepsilon_4(\omega)$ and $\varepsilon_6(\omega)$, respectively. Layer 5 denotes the medium filling in the FPI cavity, with relative permittivity ε_5.

For simplicity, here we consider $\varepsilon_1=\varepsilon_9$, $\varepsilon_2(\omega)=\varepsilon_8(\omega)$, $\varepsilon_3=\varepsilon_7$, and $\varepsilon_4(\omega)=\varepsilon_6(\omega)$. In specific calculations we will assume $\varepsilon_3=\varepsilon_7=\varepsilon_5$, as the separation h_s is mostly determined by NP-capping ligands that are embedded in the electrolytic solution. The critical step then is to determine $\varepsilon_4(\omega)$ and $\varepsilon_6(\omega)$ for estimating the optical response of each monolayer of NPs coupled to a thin metallic electrode. Within quasi-static dipolar approximation, the monolayer can be modeled as an effective film with anisotropic dielectric permittivity, which is determined by the optical polarizability of NPs, considering their mutual interactions within the array in the presence of the metallic substrate.

While forming the monolayer, the functionalized NPs, when substantially charged, would prefer to self-assemble in a hexagonal lattice. With a (=$2R+g$) as the lattice constant (where R is the NP's radius and g is the inter-NP gap), we obtain the parallel and perpendicular components of the dielectric tensor for the effective film of thickness $d=\frac{4\pi R^3}{3a^2}$ as

$$\varepsilon_6^{\parallel}(\omega)=\varepsilon_5+\frac{8\pi}{\sqrt{3a^2d}}\beta^{\parallel}(\omega), \tag{1a}$$

$$\frac{1}{\varepsilon_6^{\perp}(\omega)}=\frac{1}{\varepsilon_5}-\frac{1}{\varepsilon_5^2}\frac{8\pi}{\sqrt{3a^2d}}\beta^{\perp}(\omega), \tag{1b}$$

respectively [32]. Here, $\beta^{\parallel,\perp}(\omega)$ denotes the effective quasi-static dipolar polarizability of each NP in a monolayer while interacting with all other NPs of the 2D array along with their dipolar images on the metallic substrate, and is given by

$$\beta^{\parallel}(\omega)=\frac{\alpha(\omega)}{1+\alpha(\omega)\frac{1}{\varepsilon_5}\left[\frac{-1}{2}\frac{U_A}{a^3}-\xi\left(\frac{f(h,a)}{a^3}-\frac{3}{2}\frac{g_1(h,a)}{a^3}+\frac{1}{8h^3}\right)\right]}, \tag{2a}$$

$$\beta^{\perp}(\omega)=\frac{\alpha(\omega)}{1+\alpha(\omega)\frac{1}{\varepsilon_5}\left[\frac{U_A}{a^3}-\xi\left(\frac{f(h,a)}{a^3}-12\frac{h^2g_2(h,a)}{a^5}-\frac{1}{4h^3}\right)\right]}, \tag{2b}$$

where $\alpha(\omega)=\varepsilon_5R^3\frac{\varepsilon_{NP}(\omega)-\varepsilon_5}{\varepsilon_{NP}(\omega)+2\varepsilon_5}$ is the dipolar polarizability of an individual spherical NP of material with permittivity $\varepsilon_{NP}(\omega)$ surrounded by a medium with permittivity ε_5; $\xi=\frac{\varepsilon_5-\varepsilon_8(\omega)}{\varepsilon_5+\varepsilon_8(\omega)}$ is the image charge screening factor; and U_A, $f(h,a)$, $g_1(h,a)$, and $g_2(h,a)$ are the "lattice sums" (over a hexagonal lattice), given by

$$U_A=\sum_{i\neq0}\sum_{j\neq0}\frac{1}{(i^2+j^2-ij)^{3/2}}=11.031, \tag{3a}$$

$$f(h,a)=\sum_{i\neq0}\sum_{j\neq0}\frac{1}{\left(i^2+j^2-ij+\left(\frac{2h}{a}\right)^2\right)^{3/2}}, \tag{3b}$$

$$g_1(h,\,a)=\sum_{i\neq 0}\sum_{j\neq 0}\frac{(i^2+j^2)}{\left(i^2+j^2-ij+\left(\frac{2h}{a}\right)^2\right)^{\frac{5}{2}}}, \tag{3c}$$

$$g_2(h,\,a)=\sum_{i\neq 0}\sum_{j\neq 0}\frac{1}{\left(i^2+j^2-ij+\left(\frac{2h}{a}\right)^2\right)^{\frac{5}{2}}}, \tag{3d}$$

where $h=h_s+R$. Note that, in Eqs. (2a) and (2b), the term U_A in the denominator essentially incorporates the plasmonic interactions of each individual NP with all other NPs in the 2D hexagonal array. Considering a "reference" NP positioned at the origin, these calculations of lattice sums are carried out. The terms in the denominator, shown within parentheses, are multiplied by ξ, which accounts for the image-charge interactions effect. The functions $f(h, a)$, $g_1(h, a)$, and $g_2(h, a)$ sum up the coupling effects originating from the dipolar images of the all other NPs in the array on the "reference" NP. The last term in the parentheses with $1/h^3$ dependence includes the effects coming from the own dipolar image charges of the NP.

With the knowledge of permittivity for all the layers in our nine-layer-stack model, we then obtain the transfer matrix $\tilde{M}$, which allows the calculation of optical transmittance through the FPI. By defining the wave vectors at each layer as

$$k_1(\omega)=\frac{\omega}{c}\sqrt{\varepsilon_1}\cos\theta, \tag{4a}$$

$$k_2(\omega)=\frac{\omega}{c}\sqrt{\varepsilon_2(\omega)-\varepsilon_1\sin^2\theta}, \tag{4b}$$

$$k_3(\omega)=\frac{\omega}{c}\sqrt{\varepsilon_3(\omega)-\varepsilon_1\sin^2\theta}, \tag{4c}$$

$$k_4^{\parallel}(\omega)=\frac{\omega}{c}\sqrt{\varepsilon_4^{\parallel}(\omega)-\varepsilon_1\sin^2\theta}, \tag{4d}$$

$$k_4^{\perp}(\omega)=\frac{\omega}{c}\left(\frac{\varepsilon_4^{\parallel}(\omega)}{\varepsilon_4^{\perp}(\omega)}\right)^{1/2}\sqrt{\varepsilon_4^{\perp}(\omega)-\varepsilon_1\sin^2\theta}, \tag{4e}$$

$$k_5(\omega)=\frac{\omega}{c}\sqrt{\varepsilon_5(\omega)-\varepsilon_1\sin^2\theta}, \tag{4f}$$

$$k_6^{\parallel}(\omega)=\frac{\omega}{c}\sqrt{\varepsilon_6^{\parallel}(\omega)-\varepsilon_1\sin^2\theta}, \tag{4g}$$

$$k_6^{\perp}(\omega)=\frac{\omega}{c}\left(\frac{\varepsilon_6^{\parallel}(\omega)}{\varepsilon_6^{\perp}(\omega)}\right)^{1/2}\sqrt{\varepsilon_6^{\perp}(\omega)-\varepsilon_1\sin^2\theta}, \tag{4h}$$

$$k_7(\omega)=\frac{\omega}{c}\sqrt{\varepsilon_7(\omega)-\varepsilon_1\sin^2\theta}, \tag{4i}$$

$$k_8(\omega)=\frac{\omega}{c}\sqrt{\varepsilon_8(\omega)-\varepsilon_1\sin^2\theta}, \tag{4j}$$

$$k_9(\omega)=\frac{\omega}{c}\sqrt{\varepsilon_9(\omega)-\varepsilon_1\sin^2\theta}, \tag{4k}$$

and the phase shifts as $\delta_2=k_3h_f$, $\delta_3=k_3h_s$, $\delta_4^{(\parallel,\perp)}=k_4^{(\parallel,\perp)}d$, $\delta_5=k_5(L-2h_s-2d)$, $\delta_6^{(\parallel,\perp)}=k_6^{(\parallel,\perp)}d$, $\delta_7=k_7h_s$, $\delta_8=k_8h_f$.

A transfer matrix for the entire system can be evaluated as

$$\begin{aligned}\tilde{M}=&\frac{1}{t_{1,2}}\begin{pmatrix}e^{-i\delta_2}&r_{1,2}e^{i\delta_2}\\r_{1,2}e^{-i\delta_2}&e^{i\delta_2}\end{pmatrix}\cdot\frac{1}{t_{2,3}}\begin{pmatrix}e^{-i\delta_3}&r_{2,3}e^{i\delta_3}\\r_{2,3}e^{-i\delta_3}&e^{i\delta_3}\end{pmatrix}\cdot\\&\frac{1}{t_{3,4}}\begin{pmatrix}e^{-i\delta_4}&r_{3,4}e^{i\delta_4}\\r_{3,4}e^{-i\delta_4}&e^{i\delta_4}\end{pmatrix}\cdot\frac{1}{t_{4,5}}\begin{pmatrix}e^{-i\delta_5}&r_{4,5}e^{i\delta_5}\\r_{4,5}e^{-i\delta_5}&e^{i\delta_5}\end{pmatrix}\cdot\\&\frac{1}{t_{5,6}}\begin{pmatrix}e^{-i\delta_6}&r_{5,6}e^{i\delta_6}\\r_{5,6}e^{-i\delta_5}&e^{i\delta_6}\end{pmatrix}\cdot\frac{1}{t_{6,7}}\begin{pmatrix}e^{-i\delta_7}&r_{6,7}e^{i\delta_7}\\r_{6,7}e^{-i\delta_7}&e^{i\delta_7}\end{pmatrix}\cdot\\&\frac{1}{t_{7,8}}\begin{pmatrix}e^{-i\delta_8}&r_{7,8}e^{i\delta_8}\\r_{7,8}e^{-i\delta_5}&e^{i\delta_8}\end{pmatrix}\cdot\frac{1}{t_{8,9}}\begin{pmatrix}1&r_{8,9}\\r_{8,9}&1\end{pmatrix},\end{aligned} \tag{5}$$

where for s- and p-polarized light, the reflection and transmission coefficients, $r_{i,j}^{(s,p)}$ and $t_{i,j}^{(s,p)}$, at any interface between layers i and j, read

$$r_{ij}^{s}=\frac{k_i^{\parallel}(\omega)-k_j^{\parallel}(\omega)}{k_i^{\parallel}(\omega)+k_j^{\parallel}(\omega)}, \tag{6a}$$

$$r_{ij}^{p}=\frac{\varepsilon_i^{\parallel}k_j^{\perp}(\omega)-\varepsilon_j^{\parallel}k_i^{\perp}(\omega)}{\varepsilon_i^{\parallel}k_j^{\perp}(\omega)+\varepsilon_j^{\parallel}k_i^{\perp}(\omega)}, \tag{6b}$$

$$t_{ij}^{s}=\frac{2k_i^{\parallel}(\omega)}{k_i^{\parallel}(\omega)+k_j^{\parallel}(\omega)}, \tag{7a}$$

$$t_{ij}^{p}=\frac{2\sqrt{\varepsilon_i^{\parallel}}\sqrt{\varepsilon_j^{\parallel}}k_i^{\perp}(\omega)}{\varepsilon_i^{\parallel}k_j^{\perp}(\omega)+\varepsilon_j^{\parallel}k_i^{\perp}(\omega)}. \tag{7b}$$

The transmission coefficient $t^{(s,p)}$ from the nine-layer-stack model can be found as $t^{(s,p)}=\frac{1}{\tilde{M}_{11}}$. Finally, the percentage transmittance $T^{(s,p)}$ is calculated using

$$T^{(s,p)} = 100 \times |t^{(s,p)}|^2 \times \frac{n_9 \cos\theta_t}{n_1 \cos\theta_i}, \quad (8)$$

where $\theta_t = \sin^{-1}\left(\frac{n_1 \sin\theta_i}{n_4}\right)$ is the angle of transmission, θ_i is the angle of incidence, n_1 $(=\sqrt{\varepsilon_1})$, and n_9 $(=\sqrt{\varepsilon_9})$.

Throughout this work, we deployed spherical silver NPs and thin silver electrodes, with silver (Ag) permittivity values taken from the literature [42], while considering the cavity to be filled with an aqueous solution. Unless otherwise specified explicitly, light is assumed to enter and exit the FPI through the aqueous medium. The spacer layer is considered to have a thickness $h_s = 2$ nm. With this configuration, the results obtained using this framework are presented in the subsequent sections.

4 Results and discussion

Figure 3 depicts the transmittance, reflectance, and absorbance spectra over the spectral range 500–1100 nm of the described FPI, with the aqueous-electrolyte-filled cavity of 1 μm length. The cavity length and the spectral window are chosen at random just for demonstration of the proof-of-the-principle. The concept equally applies for other spectral ranges, extendable over the near-infrared range, and possibly beyond it, with corresponding adjustment of the cavity length and NPs' geometry and composition.

The top row of Figure 3 presents the spectra without NPs for the cavity formed between just two 20-nm-thick Ag films. Three sharp transmission peaks can be observed in the shown spectral window (Figure 3A), which correspond to the resonance states of the cavity where the reflectance is minimal (Figure 3B). The intensity of the transmission peaks depends on the resonant absorbance at that wavelength (Figure 3C). The peak absorbance tends to increase towards shorter wavelengths where the optical loss in Ag gets stronger.

The bottom row of Figure 3 shows the changes in those transmittance, reflectance, and absorbance spectra when a monolayer of silver nanospheres (of radius 10 nm and inter-particle gap of 6 nm) is assembled on each of those films. It is clearly seen in Figure 3D that the transmission peaks and reflectance minima in Figure 3E get red-shifted in the presence of the NP monolayer, but the amount of red-shifts are different for different peaks. This depends on how the reflectivity of the cavity mirrors (here, based on mirror-on-mirror nanoplasmonic metamaterial) changes with wavelength. An additional peak can be seen at short wavelengths, red-shifted to appear within the specified wavelength window (the same system without NPs has such a peak but is located below 500 nm). There are also minor changes in the finesse of the peaks. The

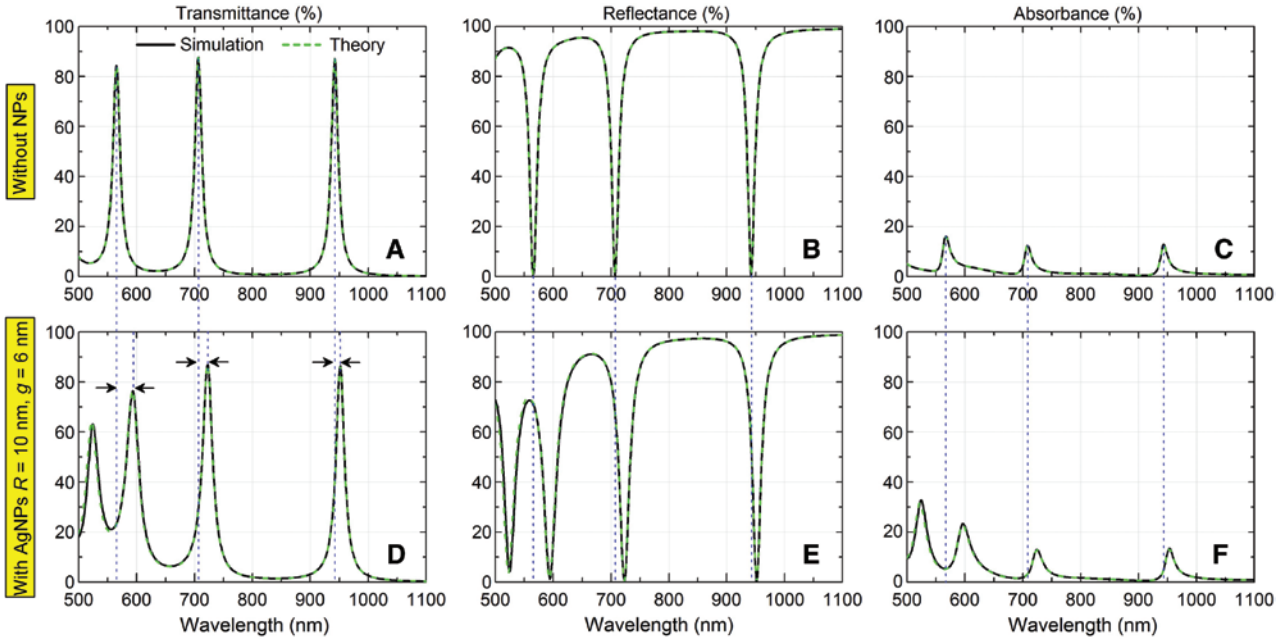

Figure 3: Study of optical properties of the proposed device.
(A and D) Transmittance, (B and E) reflectance, and (C and F) absorbance spectra from a Fabry–Perot interferometer with water-filled cavity of 1 μm length formed between two thin Ag films (20 nm thickness), without (A)–(C) and with (D)–(F) a 2D NP array of Ag nanospheres of radius $R = 10$ nm and inter-NP gap $g = 6$ nm on each of those films. Curves: black solid, full-wave simulation; green dashed, effective medium theory.

peaks towards short wavelengths tend to get slightly broader because of the strengthening of the absorbance peaks in the presence of NPs (Figure 3F).

The close correspondence of the black curves (obtained from full-wave simulations) with the dashed green curves (calculated using our theoretical framework) suggests that the theory captures all the main effects that arise from plasmonic excitations in such kind of cavities with sub-wavelength-sized NPs. For such small NPs in a not very densely packed array, higher order modes (which typically originate from the near-field coupling among neighboring NPs) are very weak and hence can be safely ignored. Therefore, our theory, which is developed on the basis of quasi-static dipolar approximation, matches perfectly well the numerical simulations.

The full-wave simulations were conducted using the RF module of the commercially available finite element method (FEM) software COMSOL Multiphysics® (COMSOL Inc., Stockholm, Sweden). Spherical Ag NPs assembling on a 20-nm-thick Ag film electrode were assumed to form a 2D hexagonal array. A simulation set-up was developed according to the schematic shown in Figure 2A, where a unit cell of the hexagonal array was modeled. Using periodic boundary conditions, the unit cell was extended in both lateral dimensions to emulate the NP monolayer assembled on each of the Ag film electrodes, those forming a cavity between them. Extremely fine meshing, with minimum element size of $\lambda/10$ (where λ is the wavelength of light in that medium), was considered so that all structural details of the system could be accurately captured in the simulations. Using the frequency domain solver over the spectral range of interest, transmittance and reflectance of the modeled system were obtained from the numerically calculated S-parameters (S_{21} and S_{11}). Absorbance in the system can be found once the transmittance and reflectance are known.

The density of NPs in the monolayer affects the reflectivity spectrum of each cavity mirror, which can be exploited for obtaining a desired transmission output from the FPI. The change in reflectivity of each cavity mirror correlates with the inter-NP gaps, i.e. it can be controlled by the density of the NP arrays. The gaps define the plasmonic coupling among the NPs. Therefore, change in gaps results in dramatic changes of the cavity transmittance peaks. Figure 4A depicts the transmission spectra for different inter-NP gaps of 3, 6, 10, and 20 nm for arrays of Ag NPs of radius $R = 10$ nm, obtained from full-wave simulations. The specific gap values were chosen to show how widely one can tune the transmission spectrum with the inter-NP gap, which will be adjusted in practice by changing the voltage applied to the thin-film electrodes.

A continuous tuning of the transmission peaks with voltage variation can thus be achieved. As can be seen, the peaks at long wavelengths experience lesser red-shift

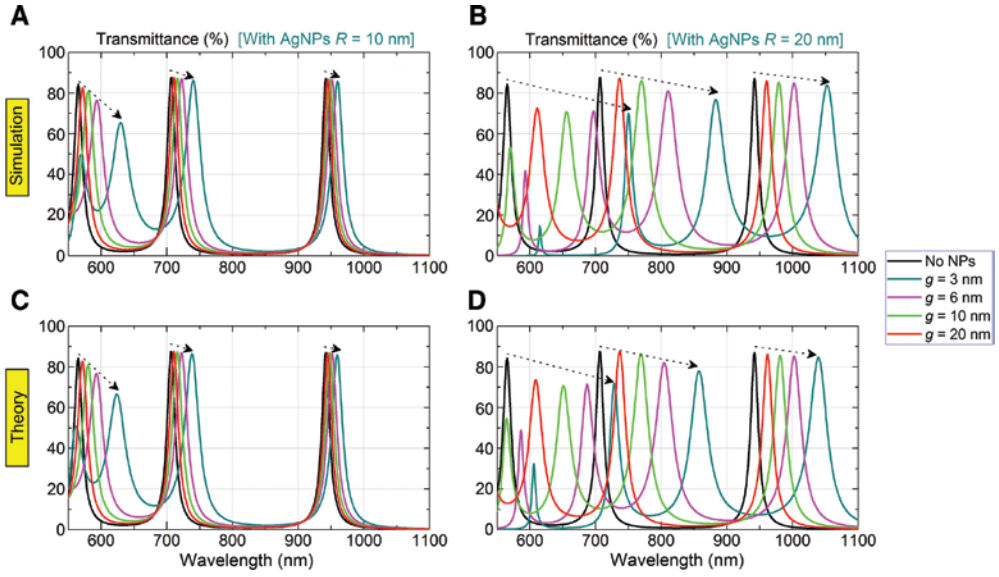

Figure 4: Tunability of transmittance characteristics.
Changes in transmittance spectrum of a Fabry–Perot interferometer (with aqueous electrolyte-filled cavity of 1 μm length) with adjustment in the inter-NP gap g in the monolayer of Ag NPs of radius $R = 10$ nm (left column) or $R = 20$ nm (right column) assembled on the inner walls of the two 20-nm-thick Ag films forming the cavity mirrors. (A, B) Top row: full-wave simulations; (C, D) bottom row: theory. In each case, black is the "reference" curve obtained for the system without NPs. Curves correspond to different indicated gaps.

than those at short wavelengths but with lesser absorption penalty on the peak transmission. The peaks are more sensitive to changes in inter-NP gaps for larger NPs, as seen for Ag NPs of radius $R = 20$ nm in Figure 4B. The transmission spectrum calculated for each of these cases based on the effective medium theory exhibits the same trend, but the theory slightly underestimates the amount of red-shift for strongly coupled plasmonic interactions when the inter-NP gap is very small (e.g. 3 nm). This can be attributed to the fact that contributions from higher order modes, induced by strong near-field coupling at small inter-NP gaps, are not considered in our theoretical model. The difference between simulation and theory due to this issue increases further for larger NPs (Figure 4C,D). With the increase in NP size, quasi-static dipolar approximation for describing the polarizability of individual NPs also becomes inadequate. Therefore, for NPs larger than 50 nm in size, the dipolar polarizability needs to be corrected by incorporating the effects of phase retardation and radiation damping [43]. However, larger NPs will not be practical because of slower mobility, as that will reduce the speed of tuning of our proposed device; but most importantly, for large NPs, of the order of 60 nm, the effects of scattering from NPs will get pronounced and the NP array will cease to behave as a continuous, smooth reflecting surface. We, therefore, choose to work with sub-wavelength-sized small NPs for this application for which our theory should and does work well.

Note that, for NPs in the same range of sizes (radius $R = 10$ or 20 nm), dipolar approximation may become inaccurate for smaller inter-NP gaps of 1–2 nm because of the emergence of higher order modes arising from intense inter-NP coupling. But such small inter-NP gaps are not relevant in our application and can be ignored. Indeed, NPs are typically capped with ligands of length ~1.5–2 nm, with charged terminal groups, so that in any case the inter-NP gaps cannot get shorter than 3 nm [33, 37]. Thus, in the considered range of inter-NP gaps, for NPs of radius $R = 10$ or 20 nm, the quasi-static dipolar approximation-based electromagnetic theory (EMT) is found to be very accurate.

Figure 5A,B re-plot Figure 4A,B, respectively, in a stacked form where the red-shifts of each transmission peak can be followed more clearly. The transmission peaks can be numbered as (i), (ii), and so on (Figure 5A), from low to high energy. It is seen that for small NPs the amount of red-shift with decrease in inter-NP gap is smaller than for large NPs. However, the peaks for smaller NPs have better finesse. By investigating the spectral shifts of each peak for both small and large NPs at similar inter-NP gaps, it can be said that the range of tunability of the peaks (i) and (ii) looks very promising.

Ideally, the transmission peak of the FPI can be tuned to any spectral position with a defined finesse by properly selecting the NP size and cavity length and then tuning the thin-film electrode potential to adjust the inter-NP gap in the NP monolayer.

The underlying mechanism of the spectral shifts of the peaks can be appreciated from Figure 6A, which plots the change in reflection coefficient r of each cavity mirror with the change in inter-NP gap, g, in the monolayer of Ag NPs of

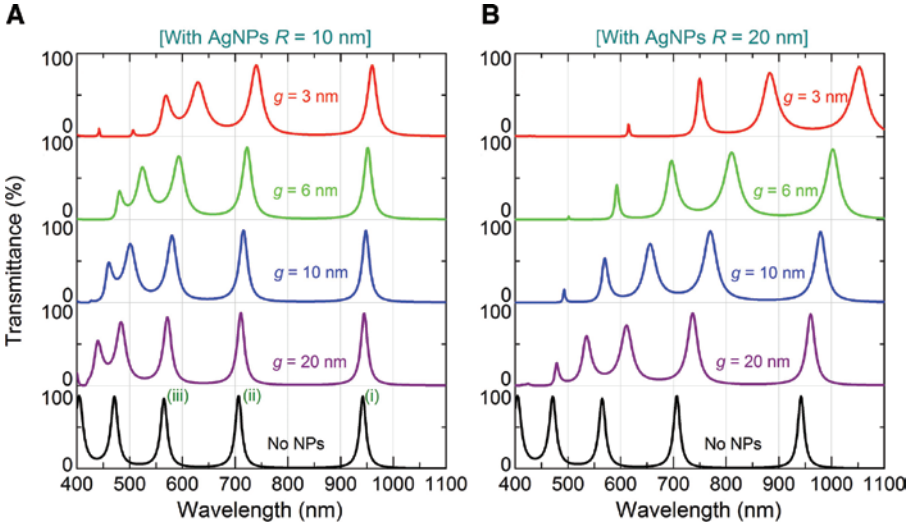

Figure 5: Tunable transmission from FPI cavity.
Transmittance spectra (obtained using full-wave simulations) from the top row of Figure 4 are presented in a stacked form, allowing clear tracking of each transmission peak with changes in inter-NP gap g in the monolayers of Ag NPs of radius $R = 10$ nm (left) and $R = 20$ nm (right).

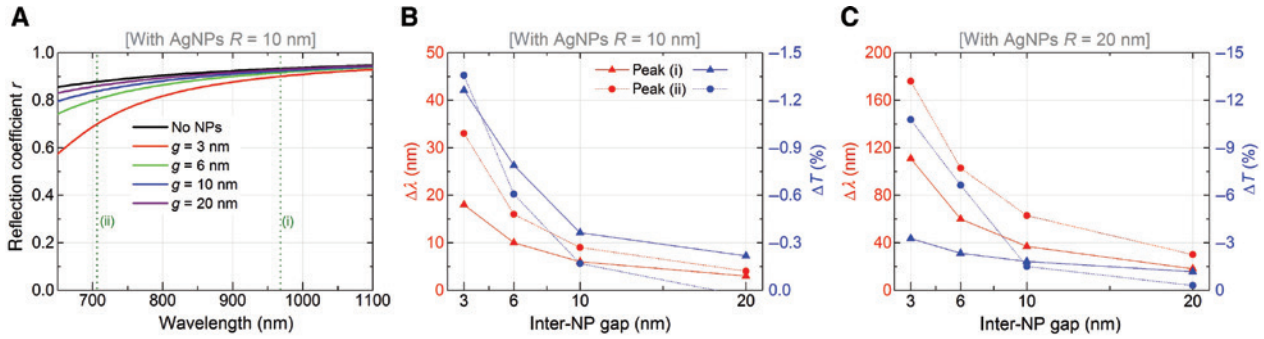

Figure 6: Influence of inter-NP gap on cavity mirror's reflectance and resulting shift in the cavity's transmittance peaks. (A) Reflection coefficient (r) of each cavity mirror, where Ag NPs of radius $R = 10$ nm are assembled to form monolayers of different density (cf. indicated inter-NP gaps) on a 20-nm-thick Ag film immersed in an aqueous electrolyte. (B) The shift in peak wavelength, $\Delta\lambda$, (in red) along with changes in transmittance percentage, ΔT, (in blue) as a function of inter-NP gaps for peaks (i) and (ii) (the peaks are those shown in Figure 4A). (C) Same as in (B) but for Ag NPs of radius $R = 20$ nm.

radius $R = 10$ nm when assembled on a 20-nm-thick Ag film dispersed in water. This allows one to track the dramatic changes in cavity mirror reflectivity at peak positions (i) and (ii), marked with the vertical dotted lines. As the change in r is more sensitive to g at lower wavelengths, peak (ii) undergoes more dramatic red-shifts compared to peak (i).

However, it is also important to maintain the transmission level of the peaks while effecting the spectral shifts. Figure 6B plots the spectral shift in wavelength ($\Delta\lambda$, in red) of each peak along with the changes in peak transmission percentage (ΔT, in blue) for different inter-NP gaps. It is seen that, with smaller gaps, although the peaks undergo a large red-shift, there could be some reduction in the peak transmission. It is recommended to have large inter-NP gaps of around 10 or 20 nm to ensure that the penalty in peak transmission is minimal. However, if more red-shift is to be achieved, one can switch to larger NPs, but one might have to pay a larger penalty in the form of reduced peak transmission (Figure 6C).

For the demonstration of the concept, Figures 3–6 depict a realization of the proposed FPI device for the case when the media through which light enters and exits the cavity are the same as the medium filling the cavity. Figure 7 shows the transmittance spectra for different surrounding/embedding medium of the FPI cavity: water, air (refractive index lesser than that of water), or fused silica (refractive index larger than that of water). The transmission peaks undergo a minor red-shift with slightly reduced intensity for air as the surrounding medium. On the other hand, for FPI devices with fused silica (or quartz) as the surrounding medium, the transmission peaks exhibit a minor blue shift with slightly increased intensity. This could be a scenario where fused silica is the substrate on which the thin Ag films are deposited. Obviously, free-standing 20 nm Ag films could be hard to realize, and we

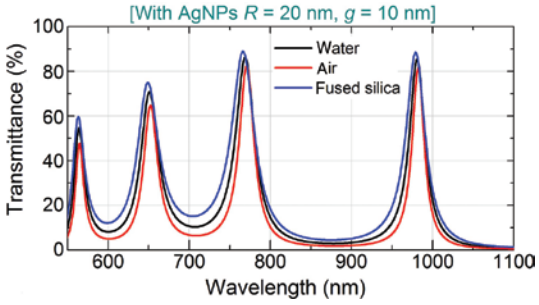

Figure 7: Transmission spectra calculated for different surrounding media: water, air, or fused silica, in which the FPI cavity is embedded. The FPI device comprises an aqueous-electrolyte-filled cavity of 1 μm length where Ag NPs of radius $R = 20$ nm assembled as a monolayer with inter-NP separation $g = 10$ nm on each of the thin Ag films (20 nm thickness) form the cavity mirrors.

have focussed on that design, in the first place, for unraveling the effects coming solely from the novel class of cavity mirrors. The essence of this analysis is that, irrespective of the surrounding medium of the FPI device, the transmission features remain qualitatively similar and will undergo tuning with electrical control on the reflectivity of the cavity mirrors, in the same way as discussed above.

5 Concluding remarks

We proposed the use of dual mirror-on-mirror nanoplasmonic metamaterials as cavity mirrors in an FPI, which allows tuning of the transmission characteristics of the FPI via controlling the inter-NP separation. Each of the cavity mirrors comprises a monolayer of NPs assembled on a thin metallic film. The thin films must be highly reflective while also allowing the incoming light to enter

and exit the cavity. The film thickness should be as low as possible, e.g. 20 nm, but can be slightly thicker or thinner.

As shown in the previous works [34, 37] of our group, such tuning can be achieved with less than 1 V variation of the electrode potential, in this case to be applied to the thin metallic films of the cavity mirrors.

The symmetry of the proposed design allows the incoming light to be incident on either of the ends, and the output can be extracted from the opposite end.

The thin-film material is not restricted to Ag but can be of any other reflective metal, e.g. Au, Al, or any other conducting material commonly used as mirrors. The thin films may have a very thin protective layer, if needed, to prevent the films from reacting with the aqueous solution. That thin protective layer may be 5 nm thick [34], or even thinner or slightly thicker, and should be conductive and transparent. This layer may also help in quick release of NPs from the metallic film surface upon alteration of electrode polarization. The NPs assembling on those thin metallic films need to carry negatively charged ligands and can be made of other less lossy plasmonic materials, if not Ag. Here, the NPs considered are of spherical shape with the radius of 10 or 20 nm, but those can be larger or smaller. The NPs can also be of any other known shapes, e.g. cubic, ellipsoidal, rods, cylindrical, etc.

The geometry of the thin metallic films at both the ends of the cavity can be of any shape, e.g. rectangle, square, polygon, or even circle. The lateral dimensions of those films should be larger than the width of the incoming beam. This requirement sets a theoretical lower limit on the lateral dimensions of the FPI device. These two films are electrically connected to form the positive electrode for the electro-tunable FPI device. The side walls of the cavity may be connected to form the opposite electrode, or the opposite electrode can be in the aqueous bulk. The cavity length, which dictates the length of the FPI device, may be chosen to achieve the transmission peaks for a desired application. Here, we used 1 μm, but it can be shorter or longer to match any desired transmission characteristics of the FPI. In other words, our proposed design of the FPI cavity is not limited to only the UV–vis range. The same concept can work for NIR and short MIR range. However, towards long MIR wavelengths, the cavity length and nanoparticle sizes may need adjustment. The device needs longer cavity and larger NPs (maybe of different composition) to operate at the long MIR range. Theoretically, the cavity length can be as small as $\lambda/2$, where λ is the wavelength of light in the cavity medium. But a shorter cavity supports fewer transmission peaks, which in turn would reduce the spectral tuning window of the transmission peaks of the FPI device. For instance, a cavity of 200 nm length, formed between two 20-nm-Ag mirrors (without NPs), supports only one transmission peak between 400 and 1500 nm, whereas, a 1-μm-length cavity supports six transmission peaks.

With positive polarization of the thin-film electrodes, the NPs (capped with negatively charged ligands) assemble on those thin metallic films in a monolayer, forming mirror-on-mirror nanoplasmonic metamaterials. The reflectivity of each of the mirror-on-mirror metamaterials can be controlled depending on the average inter-particle separation and/or their distance from the surface of the thin metallic films. Each thin-film electrode can be individually polarized, allowing the cavity to be under-coupled or over-coupled in contrast to the critically coupled cavity configuration when the two thin-film electrodes are electrically connected. The NP density can be altered by varying the electrode potential in the sub-volt regime, making such devices very energy efficient as compared to other previous electrically tunable FPIs, where several tens of volts is required for tuning.

Here, the cavity medium is an aqueous electrolytic solution, but it can be of any other electrolyte where the NPs' capping ligands can dissociate to acquire enough negative charges on their ends but could keep the NPs away from each other to avoid agglomeration.

The concept and mechanism of electro-tunability of the transmission peaks will remain unchanged for any surrounding medium of the FPI device.

Although we have shown all our results for normal incidence of the incoming light, the concept is valid for off-normal incidence angles as well.

The distance of the NPs' bottom surface from the top surface of the thin metallic films is maintained as 2 nm in the current work; however, the concept and mechanism of electro-tunability will work in the same manner for any other distances, slightly shorter or longer.

The current scheme of voltage-controlled tuning of the transmission spectrum from an FPI has been supported by our original theoretical model, which is verified successfully against commercially available full-wave simulation software. The excellent match between the two gives us a tool for optimising the FPI device structure for any specific application.

For a cavity of 1 μm length, typical transmittance adjustment time would be below, or at a maximum of, milliseconds, for very large change in the electrode potential. This can be even much shorter for very little deviation in the potential. Usually, the shorter the cavity length and the shorter the step change in applied potential, the quicker is the change in transmittance. Note that the response time is proportional to the square of the half-width of the

cavity length if there is no barrier for adsorption of NPs and their electrosorption is controlled by random diffusion, as shown in our previous work [37]. For 1 μm length and a diffusion coefficient of 5×10^{-7} cm^2/s (for NP radius $R=20$ nm), the assembly time will be $(10^{-4})^2/4\times5\times10^{-7}=5\times10^{-3}$ s. If there is a barrier for adsorption (or desorption), those limitations have to be removed by going to higher electrode potentials, which can be achieved using inorganic solvents or ionic liquids, because in aqueous solutions higher electrode potentials can cause electrolysis.

The proof-of-the-concept experiment on electro-tunability of the inter-NP gap, in a monolayer of NPs assembled on a metallic substrate, with sub-volt range variation of the electrode potential [34] corroborates the claims of the current proposal that electro-tunability in FPIs is indeed achievable with mirror-on-mirror nanoplasmonic metamaterials as cavity mirrors with ultra-low voltage variation.

Acknowledgments: DS acknowledges the support of the Marie Skodowska-Curie individual fellowship (S-OMMs), Funder Id: http://dx.doi.org/10.13039/501100000780. AAK acknowledges a grant from the Engineering and Physical Sciences Research Council UK, "Electrotuneable Molecular Alarm", EP/L02098X/1. The authors are thankful to members of the Electrochemical Nanoplasmonics team at the Chemistry Department, Imperial College (particularly Joshua Edel, Anthony Kucernak, Hayley Weir, and Ye Ma), for useful discussions.

Competing interest: The authors declare no competing financial interest.

References

[1] Vaughan JM. The Fabry–Perot interferometer. New York, NY, Routledge, 2017.
[2] Pedrotti FL, Pedrotti LM, Pedrotti LS. Introduction to optics, 3rd ed. Cambridge, UK, Cambridge University Press, 2017.
[3] Lee BH, Kim YH, Park KS, et al. Interferometric fiber optic sensors. Sensors 2012;12:2467–86.
[4] Hernández G. Fabry–Perot interferometers, 3rd ed. Cambridge, UK, Cambridge University Press, 1988.
[5] Yang J, Jiang L, Wang S, Chen Q, Li B, Xiao H. Highly sensitive refractive index optical fiber sensors fabricated by a femtosecond laser. IEEE Photon J 2011;3:1189–97.
[6] Islam M, Ali M, Lai M-H, Lim K-S, Ahmad H. Chronology of Fabry–Perot interferometer fiber-optic sensors and their applications: a review. Sensors 2014;14:7451–88.
[7] Lee CE, Markus AM, Udd E, Taylor HF. Optical-fiber Fabry–Perot embedded sensor. Opt Lett 1989;14:1225.
[8] Li M, Wang M, Li H. Optical MEMS pressure sensor based on Fabry–Perot interferometry. Opt Express 2006;14:1497.
[9] Beard PC, Mills TN. Extrinsic optical-fiber ultrasound sensor using a thin polymer film as a low-finesse Fabry–Perot interferometer. Appl Opt 1996;35:663.
[10] Yoshino T, Kurosawa K, Itoh K, Ose T. Fiber-optic Fabry–Perot interferometer and its sensor applications. IEEE Trans Microw Theory Tech 1982;30:1612–21.
[11] Rao Y-J. Recent progress in fiber-optic extrinsic Fabry–Perot interferometric sensors. Opt Fiber Technol 2006;12:227–37.
[12] Tran ATTD, Lo YH, Zhu ZH, Haronian D, Mozdy E. Surface micromachined Fabry–Perot tunable filter. IEEE Photon Technol Lett 1996;8:393–5.
[13] Kilgus J, Duswald K, Langer G, Brandstetter M. Mid-infrared standoff spectroscopy using a supercontinuum laser with compact Fabry–Pérot filter spectrometers. Appl Spectrosc 2018;72:634–42.
[14] Xu B, Liu Y, Wang D, Jia D, Jiang C. Optical fiber Fabry–Pérot interferometer based on an air cavity for gas pressure sensing. IEEE Photon J 2017;9:1–9.
[15] Çelik M, Şahin E, Yandayan T, et al. Application of the differential Fabry–Perot interferometer in angle metrology. Meas Sci Technol 2016;27:035201.
[16] Gangopadhyay TK. Prospects for Fibre Bragg Gratings and Fabry–Perot interferometers in fibre-optic vibration sensing. Sens Actuators A Phys 2004;113:20–38.
[17] Marinelli WJ, Gittins CM, Gelb AH, Green BD. Tunable Fabry–Perot etalon-based long-wavelength infrared imaging spectroradiometer. Appl Opt 1999;38:2594.
[18] Pruessner MW, Stievater TH, Ferraro MS, Rabinovich WS. Thermo-optic tuning and switching in SOI waveguide Fabry–Perot microcavities. Opt Express 2007;15:7557.
[19] Patel JS, Lee S. Electrically tunable and polarization insensitive Fabry–Perot étalon with a liquid-crystal film. Appl Phys Lett 1991;58:2491–3.
[20] Isaacs S, Placido F, Abdulhalim I. Investigation of liquid crystal Fabry–Perot tunable filters: design, fabrication, and polarization independence. Appl Opt 2014;53:H91.
[21] Patel JS, Saifi MA, Berreman DW, Lin C, Andreadakis N, Lee SD. Electrically tunable optical filter for infrared wavelength using liquid crystals in a Fabry–Perot étalon. Appl Phys Lett 1990;57:1718–20.
[22] Lin J, Tong Q, Lei Y, et al. An arrayed liquid crystal Fabry–Perot infrared filter for electrically tunable spectral imaging detection. IEEE Sens J 2016;16:2397–403.
[23] Zhang W, Ehteshami N, Liu W, Yao J. Silicon-based on-chip electrically tunable sidewall Bragg grating Fabry–Perot filter. Opt Lett 2015;40:3153.
[24] Barrios CA, Almeida VR, Panepucci RR, Schmidt BS, Lipson M. Compact silicon tunable Fabry–Pérot resonator with low power consumption. IEEE Photon Technol Lett 2004;16:506–8.
[25] Gan H, Zhang H, DeRose CT, et al. Low drive voltage Fabry–Pérot étalon device tunable filters using poled hybrid sol-gel materials. Appl Phys Lett 2006;89:041127.
[26] Wei T, Han Y, Li Y, Tsai H-L, Xiao H. Temperature-insensitive miniaturized fiber inline Fabry–Perot interferometer for highly sensitive refractive index measurement. Opt Express 2008;16:5764.
[27] Hill GC, Melamud R, Declercq FE, et al. SU-8 MEMS Fabry–Perot pressure sensor. Sens Actuators A Phys 2007;138:52–62.
[28] Helke C, Hiller K, Seiler J, et al. VIS Fabry–Pérot interferometer with structured $(TiO_2/PE\text{-}SiO_2)^3$ Bragg-reflectors on 5 mm large LP-Si_3N_4 membranes. In: Piyawattanametha W, Park Y-H, Zappe H, editors. MOEMS and miniaturized systems XVIII. USA, SPIE, 2019:25.

[29] Ran ZL, Rao YJ, Liu WJ, Liao X, Chiang KS. Laser-micromachined Fabry–Perot optical fiber tip sensor for high-resolution temperature-independent measurement of refractive index. Opt Express 2008;16:2252.
[30] Ho CP, Pitchappa P, Kropelnicki P, et al. Two-dimensional photonic-crystal-based Fabry–Perot etalon. Opt Lett 2015;40:2743.
[31] Weir H, Edel JB, Kornyshev AA, Sikdar D. Towards electrotuneable nanoplasmonic Fabry–Perot interferometer. Sci Rep 2018;8:565.
[32] Sikdar D, Hasan SB, Urbakh M, Edel JB, Kornyshev AA. Unravelling the optical responses of nanoplasmonic mirror-on-mirror metamaterials. Phys Chem Chem Phys 2016;18:20486–98.
[33] Ma Y, Zagar C, Klemme DJ, et al. A tunable nanoplasmonic mirror at an electrochemical interface. ACS Photon 2018;5:4604–16.
[34] Ma Y, Sikdar D, Fedosyuk A, et al. An auxetic thermo-responsive nanoplasmonic optical switch. ACS Appl Mater Interfaces 2019;11:22754–60.
[35] Sikdar D, Ma Y, Kucernak AR, Edel JB, Kornyshev AA. Nanoplasmonic metamaterial devices as electrically switchable perfect mirrors and perfect absorbers. In: Conference on lasers and electro-optics. California, USA, OSA, 2019:FM3C.5.
[36] Sperling RA, Parak WJ. Surface modification, functionalization and bioconjugation of colloidal inorganic nanoparticles. Philos Trans R Soc A Math Phys Eng Sci 2010;368:1333–83.
[37] Montelongo Y, Sikdar D, Ma Y, et al. Electrotunable nanoplasmonic liquid mirror. Nat Mater 2017;16:1127–35.
[38] Velleman L, Sikdar D, Turek VA, et al. Tuneable 2D self-assembly of plasmonic nanoparticles at liquid | liquid interfaces. Nanoscale 2016;8:19229–41.
[39] Velleman L, Scarabelli L, Sikdar D, Kornyshev AA, Liz-Marzán LM, Edel JB. Monitoring plasmon coupling and SERS enhancement through *in situ* nanoparticle spacing modulation. Faraday Discuss 2017;205:67–83.
[40] Zagar C, Griffith R-R, Podgornik R, Kornyshev AA. On the voltage-controlled assembly of NP arrays at electrochemical solid/liquid interfaces. 2018. Available at: http://arxiv.org/abs/1810.05019. Accessed: 20 June 2019.
[41] Sikdar D, Kornyshev AA. Theory of tailorable optical response of two-dimensional arrays of plasmonic nanoparticles at dielectric interfaces. Sci Rep 2016;6:33712.
[42] Johnson PB, Christy RW. Optical constants of the noble metals. Phys Rev B 1972;6:4370–9.
[43] Sikdar D, Rukhlenko ID, Cheng W, Premaratne M. Effect of number density on optimal design of gold nanoshells for plasmonic photothermal therapy. Biomed Opt Express 2012;4:15–31.